This is a preprint, the final version is subject to change, of the American Mineralogist (MSA)
Cite as Authors (Year) Title. American Mineralogist, in press.
(DOI will not work until issue is live.) DOI: http://dx.doi.org/10.2138/am-2015-5224

Revision 4

High-pressure behavior of cuprospinel $CuFe_2O_4$: Influence of the Jahn-Teller effect on the spinel structure

Atsushi Kyono[1,*], Stephen A. Gramsch[2], Yuki Nakamoto[3], Masafumi Sakata[3], Masato Kato[1], Tomoya Tamura[1], and Takamitsu Yamanaka[2]

[1]Division of Earth Evolution Sciences, Graduate School of Life and Environmental Sciences, University of Tsukuba, 1-1-1 Tennodai, Tsukuba, Ibaraki, 305-8572, Japan

[2]Geophysical Laboratory, Carnegie Institution of Washington, 5251 Broad Branch Road, N.W., Washington DC, 20015-1305, USA

[3]Center for Science and Technology under Extreme Conditions, Osaka University, Osaka 560-8531, Japan

Correspondence author: A. Kyono

Correspondence e-mail: kyono@geol.tsukuba.ac.jp

Phone: +81-29-853-7176, Fax: +81-29-853-7887

Revision 4

ABSTRACT

The Jahn-Teller effect at Cu^{2+} in cuprospinel $CuFe_2O_4$ was investigated using high-pressure single-crystal synchrotron X-ray diffraction techniques at beamline BL10A at the Photon Factory, KEK, Japan. Six data sets were collected in the pressure range from ambient to 5.9 GPa at room temperature. Structural refinements based on the data were performed at 0.0, 1.8, 2.7, and 4.6 GPa. The unit cell volume of cuprospinel decreases continuously from 590.8(6) $Å^3$ to 579.5(8) $Å^3$ up to 3.8 GPa. Least-squares fitting to a third-order Birch-Murnaghan equation of state yields the zero-pressure volume V_0 = 590.7(1) $Å^3$ and bulk modulus K_0 = 188.1(4.4) GPa with K' fixed at 4.0. The structural formula determined by electron microprobe analysis and site occupancy refinement is represented as $^{T}(Fe^{3+}_{0.90}Cu^{2+}_{0.10})^{M}(Fe^{3+}_{1.10}Fe^{2+}_{0.40}Cu^{2+}_{0.50})O_4$. Most of the Cu^{2+} are preferentially distributed onto the octahedrally coordinated (*M*) site of the spinel structure. With pressure, the arrangement of the oxygen atoms around the *M* cation approaches a regular octahedron. This leads to an increase in the electrostatic repulsion between the coordinating oxygen ions and the $3d_z^2$ orbital of $^{M}Cu^{2+}$. At 4.6 GPa, a cubic-tetragonal phase transition is indicated by a splitting of the *a* axis of the cubic structure into a smaller *a* axis and a longer *c* axis, with unit cell parameters *a* = 5.882(1) Å and *c* = 8.337(1) Å. The tetragonal structure with space group $I4_1/amd$ was refined to *R1* = 0.0332 and *wR2* = 0.0703 using 38 observed reflections. At the *M* site, the two *M*-O bonds parallel to the *c*-axis direction of the unit cell are stretched with respect to the four *M*-O bonds parallel to the *ab*-plane, which leads to an elongated octahedron along the *c*-axis. The cubic-to-tetragonal transition induced by the Jahn-Teller effect at Cu^{2+} is attributable to this distortion of the CuO_6 octahedron and involves Cu $3d_z^2$ orbital, *ab initio* quantum chemical calculations support the observation. At the tetrahedrally coordinated (*T*) site, on the other hand, the tetrahedral O-*T*-O bond angle increases from 109.47 ° to 111.7(7) °, which generates a compressed tetrahedral geometry along the *c*-axis. As a result of the competing distortions between the elongated octahedron and the compressed tetrahedron, the *a* unit cell parameter is shortened with respect to the *c* unit cell parameter, giving a *c*/*a*' ratio (*a*' = $\sqrt{2}$ *a*) slightly greater than unity as referred to cubic lattice (*c*/*a*' = 1.002). The *c*/*a*' value increases to 1.007 with pressure, suggesting further distortions of the elongated octahedron and compressed tetrahedron.

Keywords: cuprospinel, $CuFe_2O_4$, high-pressure, single-crystal synchrotron x-ray diffraction, Jahn-Teller effect

INTRODUCTION

The mineral spinel ($MgAl_2O_4$) adopts a slightly distorted, close-packed arrangement of oxygen atoms with magnesium and aluminum atoms distributed among the two types of interstitial sites with tetrahedral (*T*) and octahedral (*M*) coordination, respectively. In general, the spinel unit cell is composed of 32 oxygen atoms arranged in a cubic close-packed array, which forms 64 *T* sites and 32 *M* sites. In the normal spinel, divalent cations (A^{2+}) occupy one-eighth of the available *T* sites in the close-packed array, while trivalent cations (B^{3+}) occupy half of the available *M* sites, leading to the formula ${}^{T}(A^{2+}){}^{M}(B^{3+})_2O_4$, with eight formula units in the unit cell (Z = 8). In the inverse spinel, on the other hand, half of the B^{3+} cations occupy the *T* site and the remaining A^{2+} and B^{3+} cations occupy the *M* site, resulting in the formula ${}^{T}(B^{3+}){}^{M}(A^{2+}B^{3+})_2O_4$. The spinel structure is extremely flexible with regard to the variety of cations it can incorporate into both sites, as well as their distribution in the structure. At present, approximately 200 different oxides with the spinel structure have been already reported in the JCPDS-ICDD database (ICDD 2013). In particular, transition metal cations may be accomodated on both the *T* and *M* sites without any noticeable structural modification. In the unit cell of the normal spinel (space group $Fd\bar{3}m$), the *T* and *M* sites are restricted to the 8*a* (1/8, 1/8, 1/8) and 16*d* (1/2, 1/2, 1/2) Wyckoff positions, respectively, while the oxygen irons are located in the Wyckoff position 32*e* at (*u*, *u*, *u*). Hence, the spinel structure is completely described by the cubic unit cell parameter *a* and the oxygen positional parameter *u* only (e.g., Lavina et al. 2002). With $u = 1/4$, the oxygen irons are on the perfect cubic closest packing positions, but *u* generally deviates slightly from this ideal value. If displacement of the oxygen positions occurs, it is always along the [111] direction, which is aligned on the nearest *T* site. Although the spinel structure is cubic, tetragonal spinelloid phases can occur in some cases as a result of the Jahn-Teller effect imposed by the electronic states of some transition metal cations. Figure 1 shows the relationship between electronic configurations and the Jahn-Teller effect for transition metal cations in the *T* and *M* sites. If an orbital energy level is occupied in an asymmetric manner, then an orbitally degenerate state exists for that coordination environment. The Jahn-Teller theorem states that the coordination environment must distort so as to lower the symmetry and remove the degeneracy (Dunitz and Orgel, 1957; Ballhausen 1962). Because

the metal-ligand overlaps are strongest for the e_g orbitals of an octahedral complex, the Jahn-Teller effect is much more noticeable for $3d^4$ high spin (HS), $3d^7$ low spin (LS), and $3d^9$ electronic configurations, as shown in Fig. 1 (e.g., $^{[6]}Mn^{3+}$(HS), $^{[6]}Cr^{2+}$(HS), $^{[6]}Co^{2+}$(LS), $^{[6]}Cu^{2+}$). Often, these distortions are permanent and such distortions of an ideal coordination environment are generally known as "static" Jahn-Teller distortions. Similar considerations apply for the $3d^3$(HS), $3d^4$(HS), $3d^5$(LS), $3d^6$(LS), $3d^8$, and $3d^9$ configurations in a tetrahedral environment (e.g., $^{[4]}Cr^{3+}$(HS), $^{[4]}V^{2+}$(HS), $^{[4]}Mn^{3+}$(HS), $^{[4]}Cr^{2+}$(HS), $^{[4]}Fe^{3+}$(LS), $^{[4]}Mn^{2+}$(LS), $^{[4]}Co^{3+}$(LS), $^{[4]}Fe^{2+}$(LS), $^{[4]}Ni^{2+}$, $^{[4]}Cu^{2+}$). The interacting orbitals of the cations in the *T* site do not overlap effectively with those of the oxygen irons, so the interactions are relatively weaker than in the *M* site. When Jahn-Teller active cations such as Ni^{2+}, Cu^{2+}, and Mn^{3+} occupy either the *T* or *M* site in the spinel structure, a tetragonal phase occurs as a result of the Jahn-Teller distortion. Spinels with a strong Jahn-Teller distortion at the *T* site are the tetragonally distorted nichromite $NiCr_2O_4$ (Crottaz et al. 1997; Ivanov et al. 2001; Suchomel et al. 2012; Bush et al. 2013), cupric chromite $CuCr_2O_4$ (Crottaz et al. 1997; Dollase and O'Neill 1997; Kennedy and Zhou 2008; Shoemaker and Seshadri, 2010; Suchomel et al. 2012), and cupper dirhodium tetraoxide $CuRh_2O_4$ (Dollase and O'Neill 1997; Ismunandar et al. 1999). On the other hand, those with a strong Jahn-Teller distortion at the *M* site are tetragonally distorted cuprospinel $CuFe_2O_4$ (Prince and Treuting 1956; Gabal et al. 2011; Balagurov et al. 2013), hetaerolite $ZnMn_2O_4$ (Åsbrink et al. 1999; Choi et al. 2006), hausmannite $MnMn_2O_4$ (Bosi et al. 2002, 2010), and iwakiite $MnFe_2O_4$ (Matsubara et al. 1979). All of the tetragonally distorted spinels resulting from a Jahn-Teller distortion at either the *T* or *M* site have space group symmetry $I4_1/amd$, except for iwakiite ($P4_2/nnm$). These tetragonal spinelloids are of particular interest relative to the temperature effects on spin-orbital interactions as well as the influence of the Jahn-Teller effect on the crystal symmetry.

Understanding the crystal structures of earth materials under non-ambient conditions is an important step in the effort to correlate geophysical phenomena. The general pressure range of the cubic-tetragonal phase transitions in spinels suggests the possibility that such transformations may occur in the Earth's mantle. For example, chromite $FeCr_2O_4$, which contains the Jahn-Teller active Fe^{2+} ion in the *T* site, adopts the cubic structure at ambient conditions because the weak anisotropy

energy of the Fe^{2+} with $3d^6$ (HS) configuration at the *T* site is insufficient to induce the Jahn-Teller distortion. Upon compression, the Jahn-Teller effect becomes active and yields a tetrahedral angular distortion, which induces the cubic-to-tetragonal transition (Kyono et al. 2012). This pressure-induced cubic-to-tetragonal phase transition has also been observed in ulvöspinel Fe_2TiO_4 (Yamanaka et al. 2009; Kyono et al. 2011), copper manganese spinel $CuMn_2O_4$ (Waskowska et al. 2001), and lithium manganese spinel $LiMn_2O_4$ (Lin et al. 2011). Table 1 shows minerals in the spinel oxide group ($Fd\bar{3}m$) with Jahn-Teller active cations in their structures. The spinels exhibit a wide compositional variability with extensive solid solution often occurring between two endmembers. Because the physical properties of the spinels are sensitively controlled by their chemical compositions, the *P*-*T* conditions for their phase transitions are also dictated by composition. All of the spinels with end member compositions (Table 1) adopt the cubic structure at ambient conditions, but the Jahn-Teller effect is predicted to become active at either high-pressure or low-temperature resulting in tetragonally distorted structures.

Here, we report a high-pressure single-crystal synchrotron X-ray diffraction study of synthetic cuprospinel, which exhibits a strong Jahn-Teller effect at octahedrally coordinated Cu^{2+} in the spinel structure. Depending on the quenching process, only cuprospinel $CuFe_2O_4$ can exhibit both the cubic and tetragonally distorted structures under ambient conditions (e.g. Prince and Treuting 1956; Mexmain, 1971; Balagurov et al. 2013). Therefore, the cuprospinel is an appropriate sample to investigate the nature of Jahn-Teller effect, because the Cu^{2+} is both octahedrally and tetrahedrally coordinated by oxygen ions in the spinel structure. The Jahn-Teller distortion is expected to occur at not only lower temperature but also high pressure. In the present study, therefore, the structural features of pressure-induced Jahn-Teller distortion in cuprospinel are described and compared to tetragonally distorted $CuFe_2O_4$ at ambient conditions (Balagurov et al. 2013). In addition, we compare the structural modification in the cuprospinel with those in chromite and ulvöspinel, which contain Jahn-Teller active Fe^{2+}. Finally, we discuss the implication of our results in terms of their potential behavior in the Earth's mantle.

EXPERIMENTAL METHODS

Pure cuprospinel powder $CuFe_2O_4$ was synthesized from a mixture of Fe_2O_3 and Cu, which was first heated in an open quartz tube with a flowing oxygen gas stream at 1000°C for 24 h. The powder sample was then taken out of the furnace and sealed under vacuum in a quartz vessel. It was subsequently placed back into the furnace and heated again at 1300°C for 36 h, resulting in euhedral single crystals with size up to 300 μm. To identify the synthesized crystalline phase the material was ground to a fine powder using a mortar and pestle. Powder XRD data were collected with a Rigaku R-AXIS RAPID diffractometer using Mo*K*α radiation (λ = 0.70930 Å). The powder XRD profile was entirely consistent with that of a cubic $CuFe_2O_4$ phase (Mexmain 1971). No impurities were detected in the diffraction pattern.

A single crystal with well-developed faces was selected under a microscope and mounted in epoxy resin. The crystal embedded in the resin was polished with diamond plates and ultrasonically cleaned in ethanol. The sample surface was coated with carbon to improve electrical conductivity. Quantitative chemical analysis was performed using the JEOL JXA-8530F electron probe micro-analyzer (EPMA) equipped with a wavelength-dispersive X-ray spectrometer (WDS) operating at 20 kV acceleration voltage, 10 nA beam current, and 10 μm beam diameter. The data were reduced using a ZAF matrix correction program. For the WDS analyses, cuprite (for Cu*K*α) and hematite (for Fe*K*α) were used as standards. The single crystals synthesized in the study were found to be homogeneous within analytical error, with an average chemical composition (13 analyses within the grain) of 20.0(3) wt% CuO, 79.2(1.1) wt% FeO_{tot}, and total 99.2(1.2) wt%. The contents of Fe^{2+} and Fe^{3+} were calculated by charge balance on a stoichiometric basis. On the basis of a total of four oxygen atoms, the empirical formula of the cuprospinel crystal is $Cu^{2+}_{0.599}(Fe^{2+}_{0.401}Fe^{3+}_{2.000})_{\Sigma 2.401}O_4$.

After the EPMA measurement, the crystal was further polished carefully to a thickness of 35 μm for high-pressure x-ray diffraction experiments. The single crystal (dimensions of approximately 80 × 80 × 35 μm) was mounted in a diamond anvil cell equipped with two Boehler-Almax diamonds and tungsten carbide seats. The culet size of the diamonds was 300 μm. The crystal was placed into a

steel gasket hole of 150 μm diameter with a 16:3:1 mixture of methanol-ethanol-water, which remains hydrostatic up to about 9.5 to 10 GPa (Angel et al. 2007). A ruby chip was also loaded into the sample chamber for pressure calibration using the wavelength shift of the ruby luminescence (Mao et al. 1986).

The high-pressure single-crystal synchrotron X-ray diffraction study was carried out using a high-resolution, vertical-type four-circle diffractometer and scintillation counter installed at BL-10A at the Photon Factory, High Energy Accelerator Research Organization (KEK), Tsukuba, Japan. The incident wavelength was selected with a Si(111) crystal and collimated by a 0.3 mm circular pinhole. The wavelength determined by calibration using the unit cell parameters of the ruby standard (NIST Standard Reference Material #1990) was 0.71361(2) Å. Unit cell parameters of the sample were determined by a least-squares refinement of the setting angles of 15–25 centered reflections with 20° < 2θ < 30°. A total of 7 high-pressure data collections (P = 0.0, 1.8, 2.7, 3.8, 4.6, 5.9, and 6.8 GPa) were carried out. At a pressure of 6.8 GPa, however, the measurement did not result in acceptable intensity data because some diffuse spots appeared in the data. For crystal structural refinements, intensity data collections were performed at 0.0, 1.8, 2.7, and 4.6 GPa using the φ-fixed / ω-scan mode, with a scan width of 0.8° in ω, and a step interval of 0.01°. Intensity data were integrated by the full-profile fitting program WinIntegrStp (Angel 2003) and corrected for Lorentz and polarization effects. Absorption effects were however neglected in view of the small crystal size. The crystal structures were refined using the SHELXL-97 program suite (Sheldrick 1997). X-ray reflection intensity data with $F_o > 4.0\sigma(F_o)$ were used for all structural refinements, where F_o is the structure factor for each observed reflection and $\sigma(F_o)$ is the standard deviation for each F_o. At 0.0 GPa, the site-occupancy parameters of the *T* and *M* sites were refined based on the results of electron microprobe analysis. The cation distributions of Cu/Fe between the *T* and *M* sites suggested that the *T* site is filled with 90(1) % Fe and 10(1) % Cu, whereas the *M* site is with 75(1) % Fe and 25(1) % Cu. The crystal-chemical composition is therefore represented as $^{T}(Fe_{0.90}Cu_{0.10})^{M}(Fe_{1.50}Cu_{0.50})O_4$. In addition, it is apparent that small quantities of Fe^{2+} are incorporated into the cuprospinel sample as a result of the synthetic method. Although the distribution of Fe^{2+} and Fe^{3+} among the *T* and *M* sites was

not refined in this study, Fe^{2+} is recognized to have a larger octahedrally coordinated site preference than Fe^{3+} in the $CuFe_2O_4$ due to the larger ionic radius of Fe^{2+} (0.770Å) compared with Fe^{3+} (0.645 Å) (Thapa et al. 2010). For this reason, it was assumed that all Fe^{2+} cations preferentially occupy the *M* site. Taking into account charge balance based on four oxygen atoms per formula unit, the composition of the sample is represented as $^{T}(Fe^{3+}_{0.90}Cu^{2+}_{0.10})^{M}(Fe^{3+}_{1.10}Fe^{2+}_{0.40}Cu^{2+}_{0.50})O_4$. In this study, all atomic positions were refined with equivalent temperature factors (U_{iso}).

Ab initio quantum chemical calculation of the electronic structure of cuprospinel was performed with the DFT/B3LYP/6-311+G(d) basis set using the quantum chemical package Gaussian-09 (Frisch et al. 2009). Structural models were built based on the atomic coordinates experimentally determined by the single-crystal X-ray diffraction measurement at 4.6 GPa. The *T* sites were assumed to be fully occupied by Fe^{3+}, whereas the *M* sites are occupied by both Fe^{3+} and Cu^{2+}. The dimensions of the simulation region was approximately 8.1 × 5.9 × 5.9 Å, which includes two $Fe^{3+}O_4$ tetrahedra, two $Fe^{3+}O_6$ octahedra, and two $Cu^{2+}O_6$ octahedra. To terminate the infinite crystal structure, hydrogen was added as a positive charge on the oxygen irons at the terminal positions. The simulated structure model of the tetragonally distorted cuprospinel is composed of two Cu^{2+}, four Fe^{3+}, 22 O^{2-}, and 36 H^{+} with 8 positive charges. The orbital surfaces were rendered with the GaussView molecular visualization package (Dennington et al. 2009). In order to further clarify the difference in Jahn-Teller distortions between the *M* site and the *T* site, *ab initio* calculation of electronic structure of chromite $FeCr_2O_4$ was also performed in the same manner. Structural models were based on the atomic coordinates at 13.7 GPa as determined by Kyono et al. (2012).

RESULTS

Crystal structure variation of cuprospinel with pressure

The pressure variation of unit cell parameters is listed in Table 2. Details of crystal structure refinements, final atomic coordinates, isotropic thermal parameters, bond distances, and bond angles are given in Table 3. The variations in volume and unit cell parameters with pressure are shown in Figure 2. In order to provide a convenient reference between cubic and tetragonal structures, the

volume of the tetragonal lattice is doubled in Figure 2a. The *a* unit cell parameter in the tetragonal lattice is multiplied by $\sqrt{2}$ in Figure 2b. At 4.6 GPa, the *a* lattice parameter of 8.325(5) Å was obtained by least squares refinement of the observed peak positions. The measured pressure–volume curve of cuprospinel shows a slight discontinuity at this pressure. Miller indices for the cubic *F*-lattice are therefore reassigned to those corresponding to a tetragonal *I*-lattice through the transformation matrix (1/2, -1/2, 0) (1/2, 1/2, 0) (0, 0, 1). The structural relationship between the cubic *F*-lattice and the tetragonal *I*-lattice is shown in Figure 3. Unit cell parameters for the tetragonal lattice were a = 5.882(1) Å (the pseudo-cubic *a*-axis length multiplied by $\sqrt{2}$ was 8.318 Å), c = 8.337(1) Å, and V = 288.5(1) Å^3. The unit cell parameter of 8.337(4) Å at 3.8 GPa was also recalculated by the Miller indices of the tetragonal *I*-lattice. However, the obtained unit cell parameters a = 5.895(1) Å (the pseudo-cubic *a*-axis length, $a' = \sqrt{2}\,a$, was 8.337 Å) and c = 8.340(1) Å were approximately equal to the unit cell parameter of the cubic lattice, 8.337(4) Å, within the standard deviation. Accordingly, it can be concluded that the phase transition from cubic to tetragonal occurs between 3.8 and 4.6 GPa. The pressure–volume data up to 3.8 GPa were fitted using a second-order Birch-Murnaghan equation of state, refining simultaneously the unit cell volume at room pressure V_0 and the bulk modulus K_0 using the program EOSFIT 5.2 (Angel 2002). The least squares fitting yields the zero-pressure volume V_0 = 590.7(1) Å^3 and bulk modulus K_0 = 188(4) GPa with the fixed pressure derivative K' = 4.0. These values are similar to those calculated for magnetite ($Fe^{2+}Fe^{3+}{}_2O_4$, Finger et al. 1986); V_0 = 588.0(1) Å^3, K_0 = 186(5) GPa, and K' = 4.0 (fixed), which also has both Fe^{2+} and Fe^{3+} occupying the *M* site, and Fe^{3+} on the *T* site. The crystal structure of the tetragonal cuprospinel sample at 4.6 GPa with space group $I4_1/amd$ was refined to *R1* = 0.0332, *wR2* = 0.0703 using 38 observed X-ray reflections (Table 3). In the cuprospinel, the *T* site is occupied by Fe^{3+} and Cu^{2+}, which possess the Jahn-Teller stable $(e)^2(t_2)^3$ and unstable $(e)^4(t_2)^5$ configurations, respectively. The *M* site is occupied by Fe^{3+}, Fe^{2+}, and Cu^{2+} with the Jahn-Teller stable $(t_{2g})^3(e_g)^2$, unstable $(t_{2g})^4(e_g)^2$, and unstable $(t_{2g})^6(e_g)^3$ electron configurations, respectively. The $^{M}Fe^{2+}$ can theoretically distort the coordination environment by a weak Jahn-Teller effect. Magnetite, ideally $^{T}(Fe^{3+})^{M}(Fe^{2+}{}_{1.0}Fe^{3+}{}_{1.0})_{2.0}O_4$, also

241 includes the Fe^{2+} in the *M* site. It is well known for its electron hopping between divalent and trivalent
242 iron in the *M* sites (Kündig and Hargrove 1969), resulting in the intermediate Fe valence represented
243 by $Fe^{2.5+}$ in the *M* site. Electron delocalization may reduce the weak Jahn-Teller effect at $^{M}Fe^{2+}$ in both
244 magnetite and the cuprospinel. The octahedral distortion induced by the Jahn-Teller active $^{M}Fe^{2+}$ is
245 therefore remarkably smaller than that directly induced by the Jahn-Teller effect of $^{M}Cu^{2+}$. With
246 increasing pressure, the TO_4 and MO_6 polyhedra are isotropically compressed up to 3.8 GPa. At 4.6
247 GPa, the occurrence of the Jahn-Teller distortion at Cu^{2+} leads to distorted tetrahedroa and octahedra.
248 ^{57}Fe Mössbauer spectroscopic studies show that magnetite undergoes an inverse-normal spinel
249 transition, in which Fe^{3+} occupying the *T* site are exchanged with Fe^{2+} occupying the *M* site (Pasternak
250 et al. 2004; Rozenberg et al. 2007). Since the inverse-normal spinel transition in magnetite, which is
251 accompanied by volume changes of the TO_4 and MO_6 polyhedra, occurs through an intermediate
252 configuration at least between 8 and 17 GPa, no electron charge transfer between Fe^{2+} and Fe^{3+} would
253 arise in the cuprospinel, at least at 4.6 GPa. In addition, the Jahn-Teller effect at $^{M}Cu^{2+}$ is much
254 stronger than that at $^{T}Cu^{2+}$. Hence, it is suggested that the cubic-to-tetragonal transition is induced by
255 the Jahn-Teller effect at $^{M}Cu^{2+}$. In the *M* site, the two *M*-O bonds parallel to the *c*-axis are stretched
256 compared with the four *M*-O bonds parallel to the *ab*-plane (Table 3). Consequently, the MO_6
257 polyhedron occupied by 0.55 apfu of Fe^{3+}, 0.20 apfu of Fe^{2+}, and 0.25 apfu of Cu^{2+} results in a
258 monoclinically distorted octahedron elongated along the *c*-axis (Fig. 4). At the *T* site occupied by 0.90
259 apfu of Fe^{3+} and 0.10 apfu of Cu^{2+}, on the other hand, the tetrahedral O-*T*-O (i) bond angle increases
260 from 109.47 ° to 111.7(7) °, while the O-*T*-O angle (ii) decreases to 108.4(3)° (Table 3). The
261 tetrahedral O-*T*-O (i) and O-*T*-O (ii) angles are shown in Figure 4. The tetrahedral angular distortion
262 generates a compressed tetrahedral geometry along the *c*-axis direction as shown in Figure 4, which
263 illustrates the structural relationship between the elongated MO_6 and the compressed TO_4 in the
264 tetragonally distorted spinel structure. In the spinel structure, each of the four vertices of the
265 tetrahedron is shared with vertices of octahedra aligned parallel to the *c*-axis direction. The
266 modification of the octahedral geometry along the *c*-axis direction therefore interacts directly with the
267 compression or elongation of the tetrahedral geometry along the *c*-axis direction. With the competing

268 distortions between the elongated octahedron and compressed tetrahedron along the *c*-axis direction,
269 the pseudo-cubic *a*' unit cell parameter is consequently shortened slightly more than the *c* unit cell
270 parameter in the cuprospinel. The *c*/*a*' ratio is in fact used widely as a parameter of tetragonal
271 distortion. For the cuprospinel, this distortion leads to a tetragonal elongation with a *c*/*a*' ratio of 1.002,
272 just greater than unity as referred to cubic lattice. With increasing pressure, the *c*/*a*' ratio increases to
273 1.007 (Table 2). The continuous increase of the *c*/*a*' ratio with pressure suggests further variations in
274 the compressed TO_4 and the elongated MO_6 along the *c*-axis direction. The pressure-induced phase
275 transition exhibits a compressed tetrahedron, similar to that observed in tetragonal $CuFe_2O_4$ at 293K
276 and ambient pressure by Balagurov et al. (2013).
277 Figure 5 gives the results of the *ab initio* calculation, showing the electronic orbitals in the
278 distorted coordination environment around Cu^{2+} at 4.6 GPa. In tetragonally distorted cuprospinel, the
279 electronic orbitals are much more localized on the octahedral environment of the Cu^{2+} than the
280 tetrahedral environment of the Fe^{3+}. It is evident that the Jahn-Teller distortion at the *M* site is caused
281 by the spatial distribution of the $3d_z^2$ orbitals of Cu^{2+}. It is important to mention that there is a strong
282 orbital interaction between the Cu^{2+} and O^{2-}, which has a completely antibonding orbital character.
283 Hence, the elongated octahedral geometry observed by the x-ray diffraction measurement is ascribed
284 to the repulsive interaction between the large positive and negative phases of the wavefunctions of
285 Cu^{2+} and O^{2-}, respectively.
286
287 **DISCUSSION**
288 **Jahn-Teller distortion of Cu^{2+} and Fe^{2+} in cuprospinel**
289 Tetragonally distorted $CuFe_2O_4$ at ambient conditions (Balagurov et al. 2013) shows an inverse
290 cation distribution, because the Cu^{2+} is mostly distributed into the *M* site; only 0.060 apfu Cu^{2+} are in
291 the *T* site. It is observed experimentally that the $CuFe_2O_4$ has a clear temperature dependence of the
292 unit cell parameters in the cubic and tetragonal phases. Cubic $CuFe_2O_4$, stable at high temperature,
293 transforms to the tetragonal phase below 440°C (Balagurov et al. 2013). With decreasing temperature
294 the *c*/*a*' ratio is steadily increased, and then reaches an extremely high value of 1.060 at 20°C (Table

4). The cuprospinel synthesized in this study exhibits the cubic structure at ambient condition, and has a strong preference for Cu^{2+} and Fe^{2+} at the *M* site. Therefore, the cuprospinel used in the present study can be classified as having an inverse cation distribution. Distortions of octahedral and tetrahedral coordination can be quantified using quadratic elongation and angular variance parameters (Robinson et al. 1971), which are estimated using deviations from the center-to-vertex distance and ideal angles for regular polyhedra, respectively. Upon compression, the Jahn-Teller effect at $^{M}Cu^{2+}$ yields an elongated octahedron with two longer bonds with length 2.070(9) Å along the *c*-axis than the four bonds of length 2.017(4) Å in the *ab* plane at 4.6 GPa (Table 3). It is noteworthy to mention that the angular variance parameter σ^2_{oct} at the *M* site is decreases monotonically with increasing pressure (Table 3). A similar polyhedral variation is observed in chromite (Kyono et al. 2012). The tetragonally distorted $CuFe_2O_4$ at ambient conditions investigated by Balagurov et al. (2013) shows a strongly elongated octahedron with two longer bonds of length 2.180 Å along the *c*-axis compared to the four bonds of length 1.990Å in the *ab* plane (Table 4), which results in a larger quadratic elongation parameter λ_{oct}. The angular variance parameter σ^2_{oct} for the tetragonally distorted $CuFe_2O_4$ (Balagurov et al. 2013) is, on the other hand, smaller than that of the studied cuprospinel (Table 4). With increasing pressure or decreasing temperature, therefore, the angular variance of the MO_6 octahedra decreases and the shape of the CuO_6 octahedra approaches to that of a regular octahedron. Because this structural modification causes an increase in electrostatic repulsion between the octahedrally coordinating oxygen ligands and the Cu $3d_z^2$ orbital pointing along the *c*-axis, it would consequently promote the Jahn-Teller distortion. The fact that the MO_6 octahedron with a smaller angular variance parameter forms more elongated octahedral geometry along the *c*-axis provides evidence of electrostatic repulsion between the $3d_z^2$ orbital of Cu^{2+} and the surrounding oxygen ions (Fig. 5).

The quadratic elongation parameter λ_{tet} at the *T* site remains fairly constant due to the four equal bond distances in the TO_4 tetrahedron, whereas the angular variance parameter σ^2_{tet} rises from 0.00 to 2.91 with the cubic-tetragonal phase transition (Table 3). On the other hand, approximately no angular variance at the *T* site is observed in the tetragonally distorted $CuFe_2O_4$ (Balagurov et al. 2013). This might be ascribed to the smaller amount of the Jahn-Teller active $^{T}Cu^{2+}$ (0.060 apfu).

322

323 **The cubic-to-tetragonal phase transition induced by the Jahn-Teller effect**

324 In chromite and ulvöspinel, the cubic-tetragonal phase transition and the structure modification
325 induced by the Jahn-Teller effect of Fe^{2+} has been recently investigated under high pressure and low
326 temperature (Yamanaka et al. 2009; Tsuda et al. 2010; Kyono et al. 2011, 2012). It is useful to
327 compare these results with those mentioned above. Table 4 shows some important structural and
328 polyhedral parameters in cuprospinel, chromite, and ulvöspinel, and their tetragonally distorted
329 structures.

330 Chromite, ideally $FeCr_2O_4$, has a normal cation distribution which has the *T* site fully occupied
331 by Fe^{2+} with the Jahn-Teller unstable $(e)^3(t_2)^3$ configuration, and the *M* site fully occupied by Cr^{3+}
332 with the stable $(t_{2g})^3(e_g)^0$ configuration (Dunitz and Orgel, 1960; Lenaz et al. 2004). The
333 cubic-tetragonal phase transition in chromite at either high pressure or low temperature has been
334 observed by x-ray diffraction measurements (Arima et al. 2007; Ohtani et al. 2010; Tsuda et al. 2010;
335 Kyono et al. 2012). The pressure-induced phase transition yields a tetragonally compressed lattice
336 with *c*/*a*' of 0.992 (Kyono et al. 2012). The tetrahedral O-*T*-O (i) bond angle decreases from 109.47 °
337 to 106.5(2) °, which generates an elongated tetrahedral geometry along the *c*-axis direction (Table 4).
338 This deformation of the TO_4 tetrahedron is different from that observed in the tetragonally distorted
339 cuprospinel at high pressure. In the MO_6 octahedra, on the other hand, the two *M*-O bonds parallel to
340 the *c*-axis are shortened, which leads to a compressed octahedron along the *c*-axis. The
341 low-temperature phase also shows a tetragonally compressed lattice with *c/a*' = 0.985 at 90 K (Tsuda
342 et al. 2010). As a result of the Jahn-Teller distortion at the FeO_4 tetrahedron, the O-*T*-O (i) angle
343 increases from 109.47 ° to 111.8(1) °, which gives a compressed tetrahedral geometry along the *c*-axis
344 (Table 4). With the compressed tetrahedral geometry, consequently, the octahedral coordination
345 geometry is forced to elongate along the *c*-axis direction. As shown in Figure 4, the competition for
346 the axial elongation and compression of the MO_6 and TO_4 contributes to the tetragonal deformation
347 (*c*/*a*') of the lattice. A variation in tetragonal deformation can be therefore characterized by the

cooperative nature between elongation and compression of the coordination polyhedra along the *c*-axis direction.

Figure 6 shows the result of *ab initio* calculations with respect to the electronic orbitals of $^{T}Fe^{2+}$ in the tetragonally distorted chromite at 13.7 GPa, and gives the important suggestion that the $3d_{xy}$ orbital of Fe^{2+} is slightly tilted from the *ab*-plane in the structure. The position of the $3d_{xy}$ orbital can cause the TO_4 tetrahedron to either elongate or compress along the *c*-axis direction, depending on the electrostatic repulsion between the $3d_{xy}$ orbital and the oxygen ions. In general, interacting orbitals on Jahn-Teller active cations in the *T* site do not overlap effectively with anions compared with the case in the *M* site, so the interaction in *T* site is relatively weaker than in the *M* site (Dunitz and Orgel, 1957; Ballhausen 1962). None of 3*d* orbitals points to the tetrahedral arrangement of four ligands when the $3d_{xy}$, $3d_{yz}$, and $3d_{zx}$ orbitals are parallel to the *ab*-plane, *bc*-plane, and *ac*-plane, respectively. However, the tilt of the $3d_{xy}$ orbital causes an electrostatic repulsion between the tetrahedrally coordinating oxygen ions and the $3d_{xy}$ orbital, which is responsible for the Jahn-Teller distortion around the $^{T}Fe^{2+}$. Because no angular distortion occurs at the *T* site during compression, only contraction of the *T*-O bond length triggers the electrostatic repulsion between the tetrahedrally coordinated oxygen ligands and the $3d_{xy}$ orbital of Fe^{2+}.

Figure 7 illustrates the structural deformation mechanisms caused by the electrostatic repulsion between oxygen ions and the 3*d* orbitals of Jahn-Teller active cation in the tetragonally distorted spinels. In chromite, with increasing pressure the tetrahedrally coordinated oxygen ions are moved away from the $3d_{xy}$ orbital by the decreasing O-*T*-O (i) angle and reduce the repulsion between oxygen ions and the $3d_{xy}$ orbital (Fig. 7b). This structural variation leads to the elongated TO_4 tetrahedron and the compressed MO_6 octahedron. With decreasing temperature, on the other hand, the tetrahedrally coordinated oxygen ions are moved away from the $3d_{xy}$ orbital by increasing the O-*T*-O (i) angle (Fig. 7c), which results in the compressed TO_4 and the elongated MO_6. The different directions in which the oxygen irons move are responsible for the elongated MO_6 in chromite.

All of the *T* sites and half of *M* sites in ulvöspinel, with the ideal formula of Fe_2TiO_4, are occupied by the Jahn-Teller active Fe^{2+} with the Jahn-Teller unstable $(e)^3(t_2)^3$ and $(t_{2g})^4(e_g)^2$

375 configurations, respectively, due to its inverse spinel structure (Bosi et al. 2009). It is well known that
376 ulvöspinel is transformed from the cubic to tetragonal structure with either increasing pressure or
377 decreasing temperature (e.g., Ishikawa and Syono, 1971, Yamanaka et al. 2009). At high pressure, the
378 structure transforms to a tetragonally compressed phase with $c/a' = 0.988$ (Yamanaka et al. 2009). The
379 MO_6 octahedron adopts the compressed geometry with the shorter *M*-O bonds along the *c*-axis,
380 whereas the TO_4 tetrahedron adopts the elongated geometry with decreased O-*T*-O (i) bond angles
381 (Table 4). The deformation relationship between the MO_6 and TO_4 is also opposite to that for
382 cuprospinel. At low temperature, the structure changes to a subtly elongated lattice with c/a' ratio =
383 1.004 (Table 4). All the *M*-O bond distances in the MO_6 octahedron are essentially identical within
384 experimental uncertainties. The TO_4 tetrahedron adopts a slightly elongated geometry at low
385 temperature. In this case, the Jahn-Teller effect is not clearly observed at low temperature as a result
386 of the low electrostatic repulsion between the oxygen ions and the 3*d* orbitals of Fe^{2+} (Kyono et al.
387 2012). In addition, the fact that half of the *M* sites in the ulvöspinel are occupied with Fe^{2+} and the
388 other half with Ti^{4+} which is a Jahn-Teller inactive cation, might partly obscure the distortion.
389 Although Yamanaka et al. (2009) stated that in ulvöspinel the cubic-tetragonal transition is induced by
390 the Jahn-Teller effect at $^{T}Fe^{2+}$, the bond distance and bond angles in the TO_4 tetrahedron shown in
391 Table 4 suggest that the Jahn-Teller effect at $^{T}Fe^{2+}$ is fairly small. In the case of ulvöspinel, the
392 compressed MO_6 may be due to the electrostatic repulsion between oxygen ions and the $3d_{x^2-y^2}$ orbital
393 of Fe^{2+}, but further work is needed to clarify this point.
394
395 **IMPLICATIONS**
396 The mantle transition zone in the Earth is an anomalous region between about 400 and 750 km
397 depth in which density and seismic velocities increase much more steeply than in the surrounding
398 mantle, with particularly sharp changes noted near depths of 410, 520, and 660 km. The 660 km
399 seismic discontinuity divides the upper and lower mantle, and is usually attributed to the post-spinel
400 transition boundary where ringwoodite with spinel-type structure decomposes to Mg–perovskite and
401 ferropericlase in a peridotite mantle composition. Seismological studies, however, suggest that its

depth varies considerably in different regions (e.g. Petersen et al., 1993; Flanagan and Shearer, 1998; Helffrich, 2000; Li and Yuan, 2003; Hetényi et al., 2009; Wang and Niu, 2010; Cornwell et al., 2011). One of the effects proposed to explain these seismic observations is chemical heterogeneity within the mantle (Rigden et al. 1991; Gu et al. 1998; Cornwell et al. 2011; Schmerr and Thomas, 2011).

Spinels crystallize over a wide range of conditions from mafic and ultramafic magma, and also exhibit a wide range of solid solution. Among the spinels, chromite is usually one of the first phases to crystallize from mafic–ultramafic magmas and is a powerful petrological and geodynamic indicator (Irvine 1965, 1967; Dick and Bullen, 1984; Sack and Ghiorso, 1991a; Barnes and Roeder, 2001). A comprehensive model for the thermodynamic properties of $(Mg,Fe^{2+})(Fe^{3+},A1,Cr)_2O_4$–$(Mg,Fe^{2+})_2TiO_4$ spinels completely covers the composition space of principal petrological interest (Sack and Ghiorso, 1991b; Ghiorso and Sack, 1995). With increasing pressure, in the spinel structure the geometry of the coordinated oxygen irons approaches a regular octahedron, which leads to an increase in electrostatic repulsion between the coordinating oxygen ligands and a central Jahn-Teller active cation. Therefore, the Cu^{2+} and Fe^{2+} cations, potentially having the Jahn-Teller effect, are predicted to distort, which can lead to tetragonally distorteded structures with pressure. The Earth's upper mantle contains both ferric and ferrous irons but ferrous iron is by far the more dominant species (e.g., Canil and O'Neill, 1996; Woodland and Koch, 2003; McCammon and Kopylova, 2004; Frost and McCammon, 2008). The acoustic properties of spinels containing Fe^{2+} will vary with crystal structure, and it is therefore expected that the cubic and tetragonal phases of Fe-containing spinels differ in their acoustic properties. By including the effects of the Jahn-Teller distortion in models of mantle heterogeneity, the correspondence between models of mantle dynamics and observations from seismic tomography could potentially be improved.

ACKNOWLEDGEMENTS

The authors thank F. Bosi and two anonymous reviewers for their many constructive and helpful comments that significantly improved the quality of this paper. H. Kojitani is acknowledged for editorial handling and useful suggestions. The authors would like to thank N. Chino for kindly providing technical help with the EPMA analyses. This work was supported by a Grant-in-Aid for Young Scientists (B) from the Japan Society for the Promotion of Science (project no. 24740352). The synchrotron XRD measurements were performed at the KEK-PF with the approval of the Photon Factory Program Advisory Committee (Proposal No 2013G046 and No 2013G554).

REFERENCES CITED

Angel, R.J. (2002) EOSFIT V5.2. Crystallography laboratory. Department of Geological Sciences, Virginia Tech, USA.

Angel, R.J. (2003) Automated profile analysis for single-crystal diffraction data. Journal of Applied Crystallography, 36, 295–300.

Angel, R.J., Bujak, M., Zhao, J., Gatta, D., and Jacobsen, S.D. (2007) Effective hydrostatic limits of pressure media for high-pressure crystallographic studies. Journal of Applied Crystallography, 40, 26–32.

Arima, T., Watanabe, Y., Taniguchi, K., Watanabe, M., and Noda, Y. (2007) Effect of Mn-substitution on magnetic and structural properties in $FeCr_2O_4$. Journal of Magnetism and Magnetie Materials, 310, 807–809.

Åsbrink, S., Waśkowska, A., Gerward, L., Staun Olsen, J., and Talik, E. (1999) High-pressure phase transition and properties of spinel $ZnMn_2O_4$. Physical Review, B60, 12651–12656.

Balagurov, A.M., Bobrikov, I.A., Maschenko, M.S., Sangaa, D., and Simkin, V.G. (2013) Structural phase transition in $CuFe_2O_4$ spinel. Crystallography Reports, 58, 710–717.

Ballhausen, C. J. (1962) Introduction to Ligand Field Theory. New York, McGraw-Hill, Chapter 7.

Barnes, S.J. and Roeder, P.L. (2001) The range of spinel compositions in terrestrial mafic and ultramafic rocks. Journal of Petrology, 42, 2279–2302.

Bosi, F., Lucchesi, S., and Della Giusta, A. (2002) Structural relationships in $(Mn_{1-x}Zn_x)Mn_2O_4$ ($0 \leq x \leq 0.26$): the "dragging effect" of the tetrahedron on the octahedron. American Mineralogist, 87, 1121–1128.

Bosi, F., Hålenius, U., and Skogby, H. (2009) Crystal chemistry of the magnetite-ulvöspinel series. American Mineralogist, 94, 181–189.

Bush, A.A., Shkuratov, V.Y., Kamentsev, K.E., Cherepanov, V.M. (2013) Preparation and X-ray diffraction, dielectric, and Mossbauer characterization of $Co_{1-x}Ni_xCr_2O_4$ solid solutions. Inorganic Materials, 49, 296–302.

462 Canil, D. and O'Neill, H.S.C. (1996) Distribution of ferric iron in some upper-mantle assemblages.
463 Journal of Petrology, 37, 609–635.
464 Cornwell, D.G., Hetényi, G., Blanchard, T.D. (2011) Mantle transition zone variations beneath the
465 Ethiopian rift and Afar: chemical heterogeneity within a hot mantle? Geophysical Research
466 Letters, 38, L16308.
467 Crottaz, O., Kubel, F., and Schmid, H. (1997) Jumping crystals of the spinels $NiCr_2O_4$ and $CuCr_2O_4$.
468 Journal of Materials Chemistry, 7, 143–146.
469 Dennington, R., Keith, T., Millam, J. (2009) GaussView, Version 5, Semichem Inc., Shawnee Mission
470 KS.
471 Dick, H.J.B. and Bullen, T. (1984) Chromian spinel as a petrogenetic indicator in abyssal and
472 alpine-type peridotites and spatially associated lavas. Contributions to Mineralogy and
473 Petrology, 86, 54–76.
474 Dollase, W.A. and O'Neill, H.S. (1997) The spinels $CuCr_2O_4$ and $CuRh_2O_4$. Acta Crystallographica,
475 C53, 657–659.
476 Dunitz, J.D. and Orgel, L.E. (1957) Electronic properties of transition-metal oxides—I: Distortions
477 from cubic symmetry. Journal of Physics and Chemistry of Solids, 3, 20–29.
478 ---------- (1960) Stereochemistry of ionic solids. Advances in Inorganic Chemistry and
479 Radiochemistry, 2, 1–60.
480 Finger, L.W., Hazen, R.M., and Hofmeister, A.M. (1986) High-pressure crystal chemistry of spinel
481 ($MgAl_2O_4$) and magnetite (Fe_3O_4): comparisons with silicate spinels. Physics and Chemistry of
482 Minerals, 13, 215–220.
483 Flanagan, M.P. and Shearer, P.M. (1998) Global mapping of topography on transition zone velocity
484 discontinuities by stacking SS precursors. Geophysical Research Letters, 103, 2673–2692.
485 Frisch, M.J., Trucks, G.W., Schlegel, H.B., Scuseria, G.E., Robb, M.A., Cheeseman, J.R., Scalmani,
486 G., Barone, V., Mennucci, B., Petersson, G.A., Nakatsuji, H., Caricato, M., Li, X., Hratchian,
487 H.P., Izmaylov, A.F., Bloino, J., Zheng, G., Sonnenberg, J.L., Hada, M., Ehara, M., Toyota, K.,
488 Fukuda, R., Hasegawa, J., Ishida, M., Nakajima, T., Honda, Y., Kitao, O., Nakai, H., Vreven,

T., Montgomery, Jr.J.A., Peralta, J.E., Ogliaro, F., Bearpark, M., Heyd, J.J., Brothers, E., Kudin, K.N., Staroverov, V.N., Kobayashi, R., Normand, J., Raghavachari, K., Rendell, A., Burant, J.C., Iyengar, S.S., Tomasi, J., Cossi, M., Rega, N., Millam, J.M., Klene, M., Knox, J.E., Cross, J.B., Bakken, V., Adamo, C., Jaramillo, J., Gomperts, R., Stratmann, R.E., Yazyev, O., Austin, A.J., Cammi, R., Pomelli, C., Ochterski, J.W., Martin, R.L., Morokuma, K., Zakrzewski, V.G., Voth, G.A., Salvador, P., Dannenberg, J.J., Dapprich, S., Daniels, A.D., Farkas, Ö., Foresman, J.B., Ortiz, J.V., Cioslowski, J., Fox, D.J., (2009) Gaussian 09, Revision A.1, Gaussian, Inc., Wallingford CT

Frost, D.J. and McCammon, C.A. (2008) The redox state of Earth's mantle. Annual Review of Earth and Planetary Sciences, 36, 389–420.

Gabal, M.A., Al Angari, Y.M., and Kadi, M.W. (2011) Structural and magnetic properties of nanocrystalline $Ni_{1-x}Cu_xFe_2O_4$ prepared through oxalates precursors. Polyhedron, 30, 1185–1190.

Ghiorso, M.S. and Sack, R.O. (1995) Chemical mass transfer in magmatic processes IV. A revised and internally consistent thermodynamic model for the interpolation and extrapolation of liquid-solid equilibria in magmatic systems at elevated temperatures and pressures. Contributions to Mineralogy and Petrology, 119, 197–212.

Gu, Y., Dziewonski, A.M., and Agee, C.B. (1998) Global de-correlation of the topography of transition zone discontinuities. Earth and Planetary Science Letters, 157, 57–67.

Harrison, R.J., Redfern, S.A.T., and O'Neill, H.S.C. (1998) The temperature dependence of the cation distribution in synthetic hercynite ($FeAl_2O_4$) from in-situ neutron structure refinements. American Mineralogist, 83, 1092–1099.

Helffrich, G.R. (2000) Topography of the transition zone seismic discontinuities. Reviews of Geophysics, 38, 141–158.

Hetényi, G., Stuart, G.W., Houseman, G.A., Horváth, F., Hegedus, E., and Brückl, E. (2009) Anomalously deep mantle transition zone below Central Europe: evidence of lithospheric instability. Geophysical Research Letters, 36, L21307.

ICDD (2013) The Powder Diffraction File, Database of the International Center for Diffraction Data, 12 Campus Blvd, Newtown Square, Pennsylvania 19073–3273, USA.

Irvine, T.N. (1965) Chromian spinel as a petrogenetic indicator: Part 1. Theory. Canadian Journal of Earth Sciences, 2, 648– 672.

---------- (1967) Chromian spinel as a petrogenetic indicator: Part 2. Petrologic applications. Canadian Journal of Earth Sciences, 4, 71– 103.

Ishikawa, Y. and Syono, Y. (1971) Giant magnetostriction due to Jahn-Teller distortion in Fe_2TiO_4. Physical Review Letters, 26, 1335–1338.

Ismunandar, Kennedy, B.J., and Hunter, B.A. (1999) Phase transformation in $CuRh_2O_4$: A powder neutron diffraction study. Materials Research Bulletin, 34, 135–143.

Ivanov, V.V., Talanov, V.M., and Shabel'skaya, N.P. (2001) Phase relations in the $NiFe_2O_4$-$NiCr_2O_4$-$CuCr_2O_4$ system. Inorganic Materials, 37, 839–845.

Kennedy, B.J. and Zhou, Q. (2008) The role of orbital ordering in the tetragonal-to-cubic phase transition in $CuCr_2O_4$. Journal of Solid State Chemistry, 181, 2227–2230.

Kündig, W. and Hargrove, R.S. (1969) Electron hopping in magnetite. Solid State Communications, 7,223–227.

Kyono, A., Ahart, M., Yamanaka, T., Gramsch, S., Mao, H.K., and Hemley, R.J. (2011) High-pressure Raman spectroscopic studies of ulvöspinel Fe_2TiO_4. American Mineralogist, 96, 1193–1198.

Kyono, A., Gramsch, S.A., Yamanaka, T., Ikuta, D., Ahart, M., Mysen, B.O., Mao, H.K., and Hemley R.J. (2012) The influence of the Jahn–Teller effect at Fe^{2+} on the structure of chromite at high pressure. Physics and Chemistry of Minerals, 39, 131–141.

Lakhani, V.K., Pathak, T.K., Vasoya, N.H., and Modi, K.B. (2011) Structural parameters and X-ray Debye temperature determination study on copper-ferrite-aluminates. Solid State Sciences, 13, 539–547.

Lavina, B., Salviulo, G., and Della Giusta, A. (2002) Cation distribution and structure modelling of spinel solid solutions. Physics and Chemistry of Minerals, 29, 10–18.

Lenaz, D., Skogby, H., Princivalle, F., and Halenius, U. (2004) Structural changes and valence states in the $MgCr_2O_4$–$FeCr_2O_4$ solid solution series. Physics and Chemistry of Minerals, 31, 633–642.

Li, X.Q. and Yuan, X.H. (2003).Receiver functions in northeast China; implications for slab penetration into the lower mantle in northwest Pacific subduction zone. Earth and Planetary Science Letters, 216, 679–691.

Lin, Y., Yang, Y., Ma, H.W., Cui, Y., and Mao, W.L. (2011) Compressional behavior of bulk and nanorod $LiMn_2O_4$ under nonhydrostatic stress. Journal of Physical Chemistry C, 115, 9844–9849.

Mao, H.K., Xu, J., and Bell, P.M. (1986) Calibration of the ruby pressure gauge to 800 kbar under quasi-hydrostatic conditions. Journal of Geophysical Research, 91, 4673–4676.

Matsubara, S., Kato, A., and Nagashima, K. (1979) $Mn^{2+}(Fe^{3+},Mn^{3+})_2O_4$, a new tetragonal spinelloid mineral from the Gozaisho Mine, Fukushima Prefecture, Japan. Mineralogical Journal, 9, 383–391.

McCammon, C. and Kopylova, M. G. (2004) A redox profile of the Slave mantle and oxygen fugacity control in the cratonic mantle. Contributions to Mineralogy and Petrology, 148, 55–68.

Mexmain, J. (1971) Contribution a l'etude du ferrite cuivreux et de ses solutions solides avec le ferrite cuivrique. Annales de Chimie, 1971, 297–308.

Nii, Y., Sagayama, H., Arima, T., Aoyagi, S., Sakai, R., Maki, S., Nishibori, E., Sawa, H., Sugimoto, K., Ohsumi, H., and Takata, M. (2012) Orbital structures in spinel vanadates AV_2O_4 (A = Fe, Mn). Physical Review B, 86, 125142.

Ohtani, S., Watanabe, Y., Saito, M., Abe, N., Taniguchi, K., Sagayama, H., Arima, T., Watanabe, M., and Noda, Y. (2010) Orbital dilution effect in ferrimagnetic $Fe_{1-x}Mn_xCr_2O_4$: Competition between anharmonic lattice potential and spin-orbit coupling. Journal of Physics Condensed Matter, 22, 176003.

Pasternak, M.P., Xu, W.M., Rozenberg, G.K., Taylor, R.D., and Jeanloz, R. (2004) Pressure-induced coordination crossover in magnetite, a high pressure Mossbauer study. Journal of Physics and Chemistry of Solids, 65, 1531–1535.

Petersen, N., Gossler, J., Kind, R., Stammler, K., and Vinnik, L. (1993) Precursors to SS and structure of transition zone of the North-Western Pacific. Geophysical Research Letters, 20, 281–284.

Prince, E. and Treuting, R.G. (1956) The structure of tetragonal copper ferrite. Acta Crystallographica, 9, 1025–1028.

Rigden, S.M., Gwanmesia, G.D., FitzGerald, J.D., Jackson, I., and Liebermann, R.C. (1991) Spinel elasticity and seismic structure of the transition zone of the mantle. Nature, 354, 143–145.

Robinson, K., Gibbs, G.V., and Ribbe, P.H. (1971) Quadratic elongation: a quantitative measure of distortion in coordination polyhedra. Science, 172, 567–570.

Rozenberg, G.Kh., Amiel, Y., Xu, W.M., Pasternak, M.P., Jeanloz, R., Hanfland, M., and Taylor, R.D. (2007) Structural characterization of temperature- and pressure-induced inverse↔normal spinel transformation in magnetite. Physical Review B, 75, 020102.

Sack, R.O. and Ghiorso, M.S. (1991a) Chromian spinels as petrogenetic indicators: Thermodynamics and petrological applications. American Mineralogist, 76, 827–847.

– – – – – – – – – – – – – – – – (1991b) An internally consistent model for the thermodynamic properties of Fe- Mg-titanomagnetite-a|uminate spinels. Contributions to Mineralogy and Petrology, 106, 474–505.

Schmerr, N. and Thomas, C. (2011) Subducted lithosphere beneath the Kuriles from migration of PP precursors. Earth and Planetary Science Letters, 311, 101–111.

Sheldrick GM (1997) SHELXL97, release 97–2. Program for the refinement of crystal structures. University of Göttingen, Germany.

Shoemaker, D.P. and Seshadri, R. (2010) Total-scattering descriptions of local and cooperative distortions in the oxide spinel $Mg_{1-x}Cu_xCr_2O_4$ with dilute Jahn-Teller ions. Physical Review, B82, 214107.

Suchomel, M.R. Shoemaker, D.P., Ribaud, L., Kemei, M.C., and Seshadri, R. (2012) Spin-induced symmetry breaking in orbitally ordered $NiCr_2O_4$ and $CuCr_2O_4$. Physical Review, B86, 054406.

Thapa, D., Kulkarni, N., Mishra, S.N., Paulose, P.L., and Ayyub, P. (2010) Enhanced magnetization in cubic ferrimagnetic $CuFe_2O_4$ nanoparticles synthesized from a citrate precursor: the role of Fe^{2+}. Journal of Physics D: Applied Physics, 43, 195004.

Tsuda, K., Morikawa, D., Watanabe, Y., Ohtani, S., and Arima, T. (2010) Direct observation of orbital ordering in the spinel oxide $FeCr_2O_4$ through electrostatic potential using convergent-beam electron diffraction. Physical Review B, 81, 180102.

Uchida, H., Righter, K., Lavina, B., Nowell, M.M. Wright, S.I., Downs, R.T., and Yang, H.X. (2007) Investigation of synthetic $Mg_{1.3}V_{1.7}O_4$ spinel with MgO inclusions: Case study of a spinel with an apparently occupied interstitial site. American Mineralogist, 92, 1031–1037.

Yamanaka, T., Mine, T., Asogawa, S., and Nakamoto, Y. (2009) Jahn-Teller transition of Fe_2TiO_4 observed by maximum entropy method at high pressure and low temperature. Physical Review, B80, 134120.

Wang, B. and Niu, F. (2010) A broad 660 km discontinuity beneath northeast China revealed by dense regional seismic networks in China. Journal of Geophysical Research: Solid Earth, 115, B06308.

Waskowska, A., Gerward, L., Olsen, J.S., Steenstrup, S., and Talik, E. (2001) $CuMn_2O_4$: properties and the high-pressure induced Jahn-Teller phase transition. Journal of Physics Condensed Matter, 13, 2549–2562.

Woodland, A.B. and Koch, M. (2003) Variation in oxygen fugacity with depth in the upper mantle beneath the Kaapvaal craton, Southern Africa. Earth and Planetary Science Letters, 214, 295–310.

620

621 **Captions for Figures and Tables**

622

623 **Figure 1** The relationship between electronic configurations and the Jahn-Teller effect at transition
624 metal cations in tetrahedral and octahedral coordination. W, weak effect; S. strong effect; 0,
625 no effect.

626 **Figure 2** Variation of (a) the unit cell volume and (b) the unit cell parameters with pressure. The
627 errors are smaller than the symbols used in the figure.

628 **Figure 3** Structural relationship between the cubic *F*-lattice and the tetragonal *I*-lattice.

629 **Figure 4** Crystal structure of the tetragonally distorted cuprospinel at 4.6 GPa. The MO_6 polyhedra
630 are occupied by 0.55 Fe^{3+}, 0.20 Fe^{2+}, and 0.25 Cu^{2+}, while the TO_4 polyhedra are occupied
631 by 0.90 Fe^{3+} and 0.10 Cu^{2+}.

632 **Figure 5** Electronic orbitals in the tetragonally distorted cuprospinel at 4.6 GPa, calculated by *ab*
633 *initio* method. The red and green colors indicate positive and negative phases in the wave
634 function, respectively. The orbitals are drawn at an isosurface value of 0.02.

635 **Figure 6** Electronic orbitals in chromite at 13.7 GPa, calculated by *ab initio* method.

636 **Figure 7** Tetragonally distorted spinel induced by electrostatic repulsion between oxygen ions and
637 the 3*d* orbitals of a Jahn-Teller active cation. Structural deformations caused by (a)
638 elongation of the MO_6 along the *c*-axis in cuprospinel, (b) elongation of the TO_4 along the
639 *c*-axis in chromite and ulvöspinel at high pressure, and (c) compression of the TO_4 along
640 the *c*-axis in chromite at low temperature.

641

642 **Table 1** Minerals in spinel oxide group ($Fd\bar{3}m$) with Jahn-Teller active cations under ambient
643 conditions.

644 **Table 2** Unit cell parameters and volumes for cuprospinel at different pressures.

645 **Table 3** Structural refinement parameters and crystal structure data for cuprospinel.

646 **Table 4** Lattice parameters, selected bond distances and angles in cuprospinel, chromite, and
647 ulvöspinel measured at ambient, high pressure and low temperature conditions.

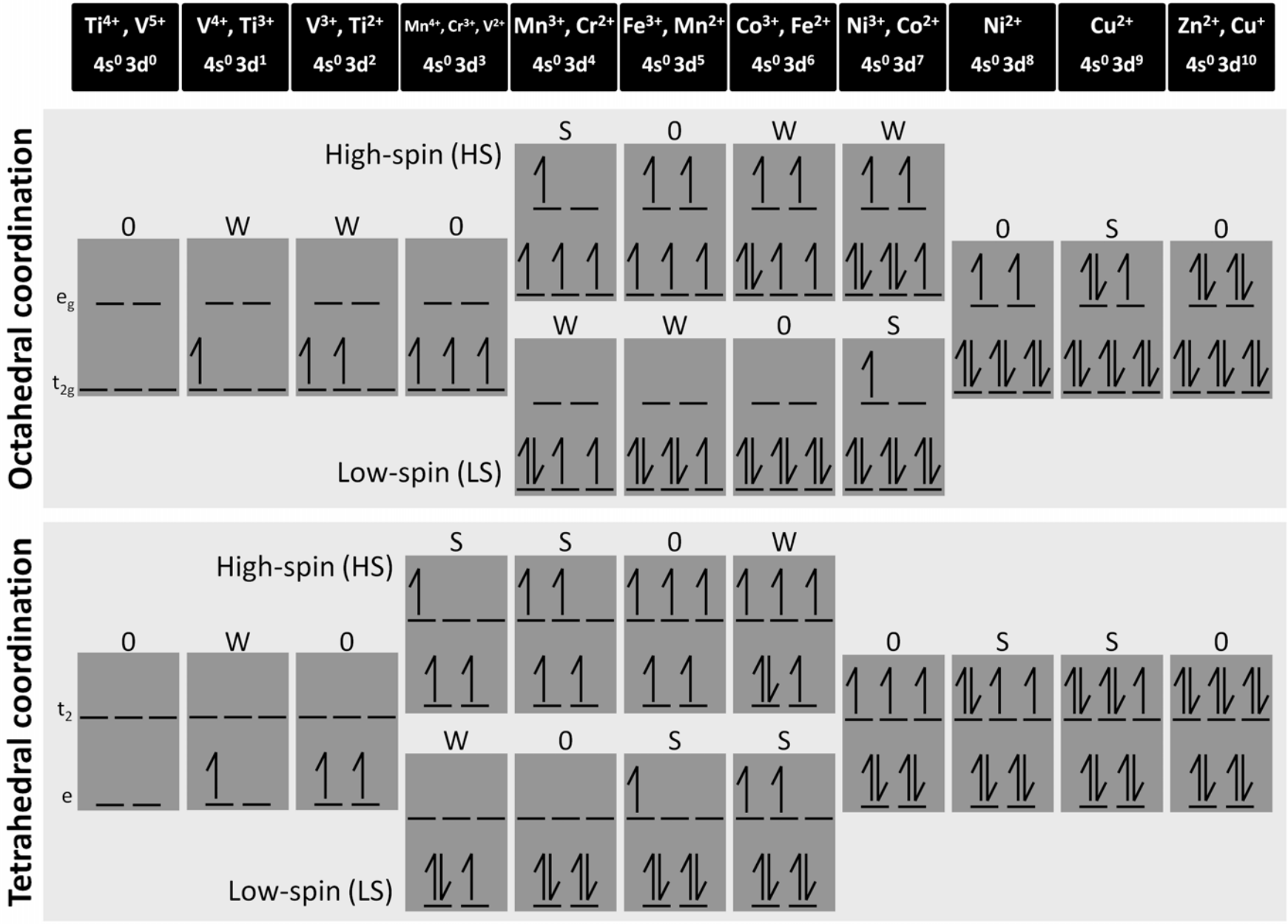

Figure 1. The relationship between electronic configurations and the Jahn-Teller effect at transition metal cations in tetrahedral and octahedral coordination. W, weak effect; S. strong effect; 0, no effect.

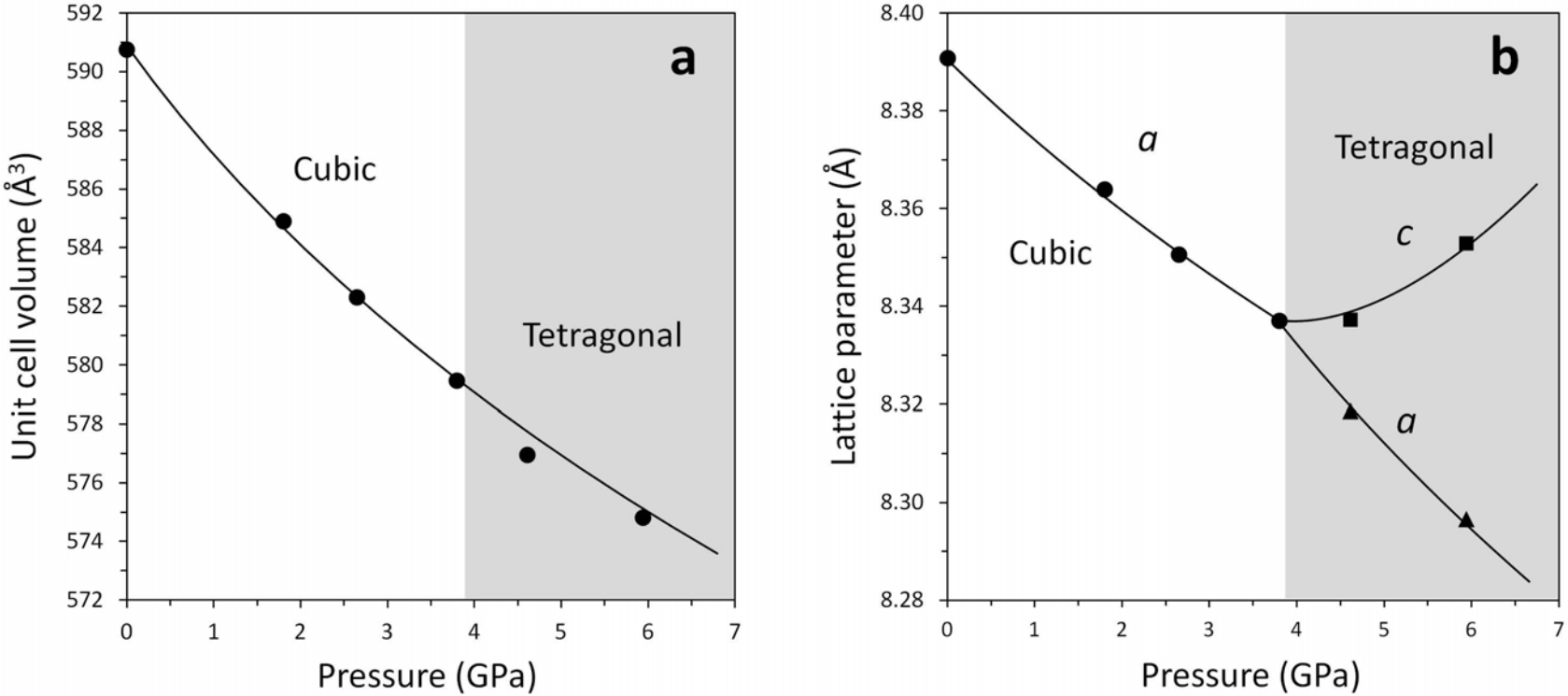

Figure 2 Variation of (a) the unit cell volume and (b) the unit cell parameters with pressure. The errors are smaller than the symbols used in the figure.

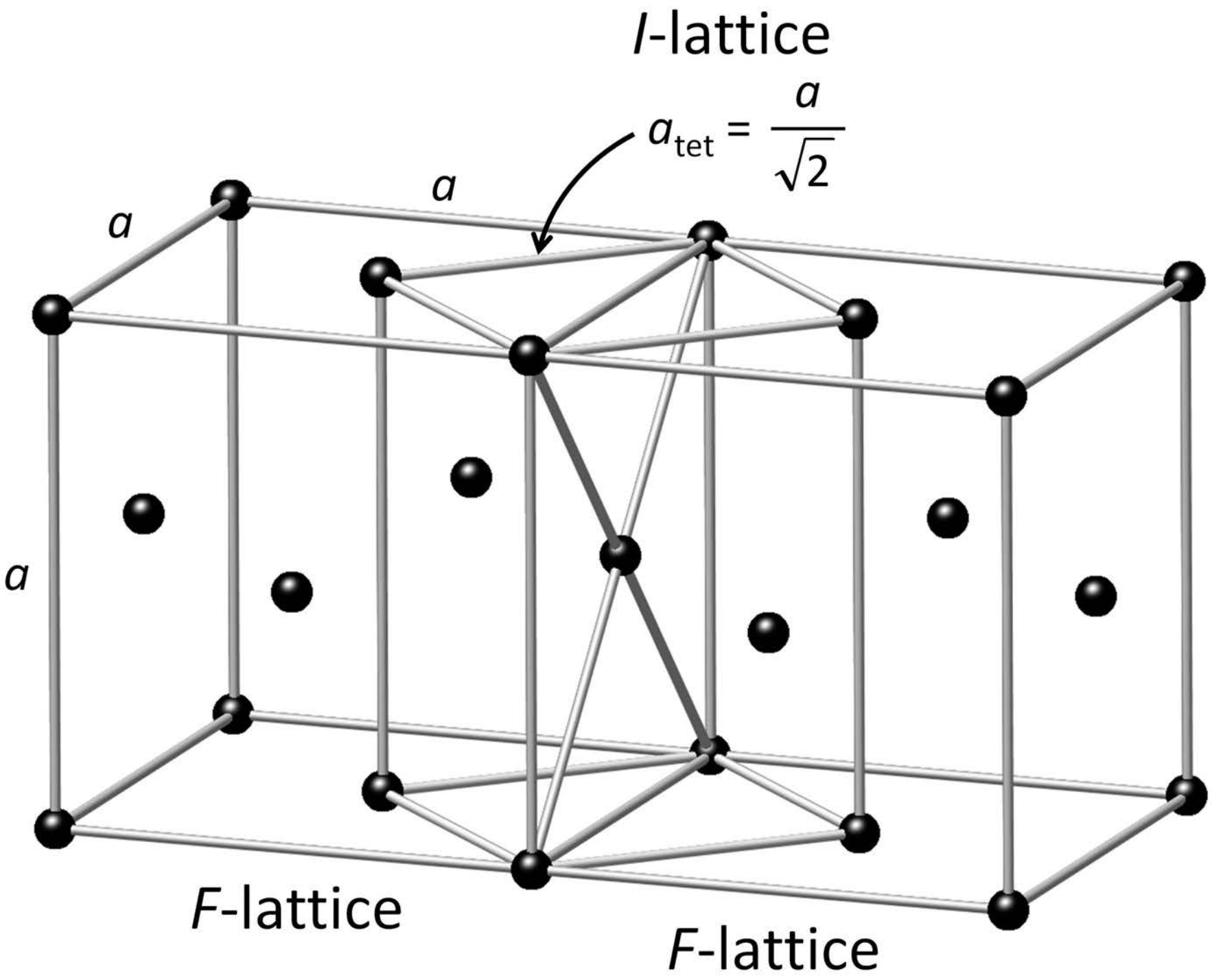

Figure 3. Structural relationship between the cubic *F*-lattice and the tetragonal *I*-lattice.

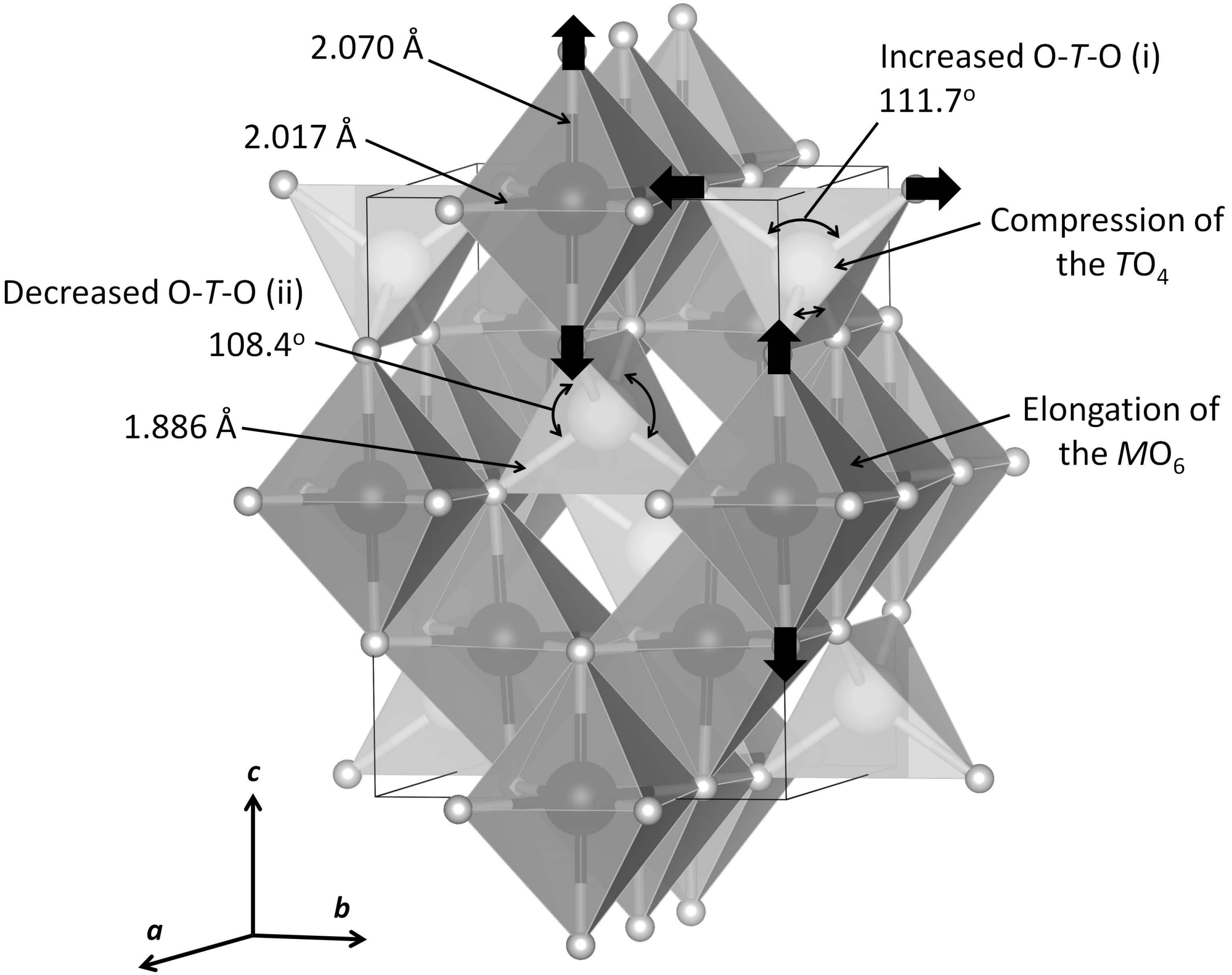

Figure 4. Crystal structure of the tetragonally distorted cuprospinel at 4.6 GPa. The MO_6 polyhedra are occupied by 0.55 Fe^{3+}, 0.20 Fe^{2+}, and 0.25 Cu^{2+}, while the TO_4 polyhedra are occupied by 0.90 Fe^{3+} and 0.10 Cu^{2+}.

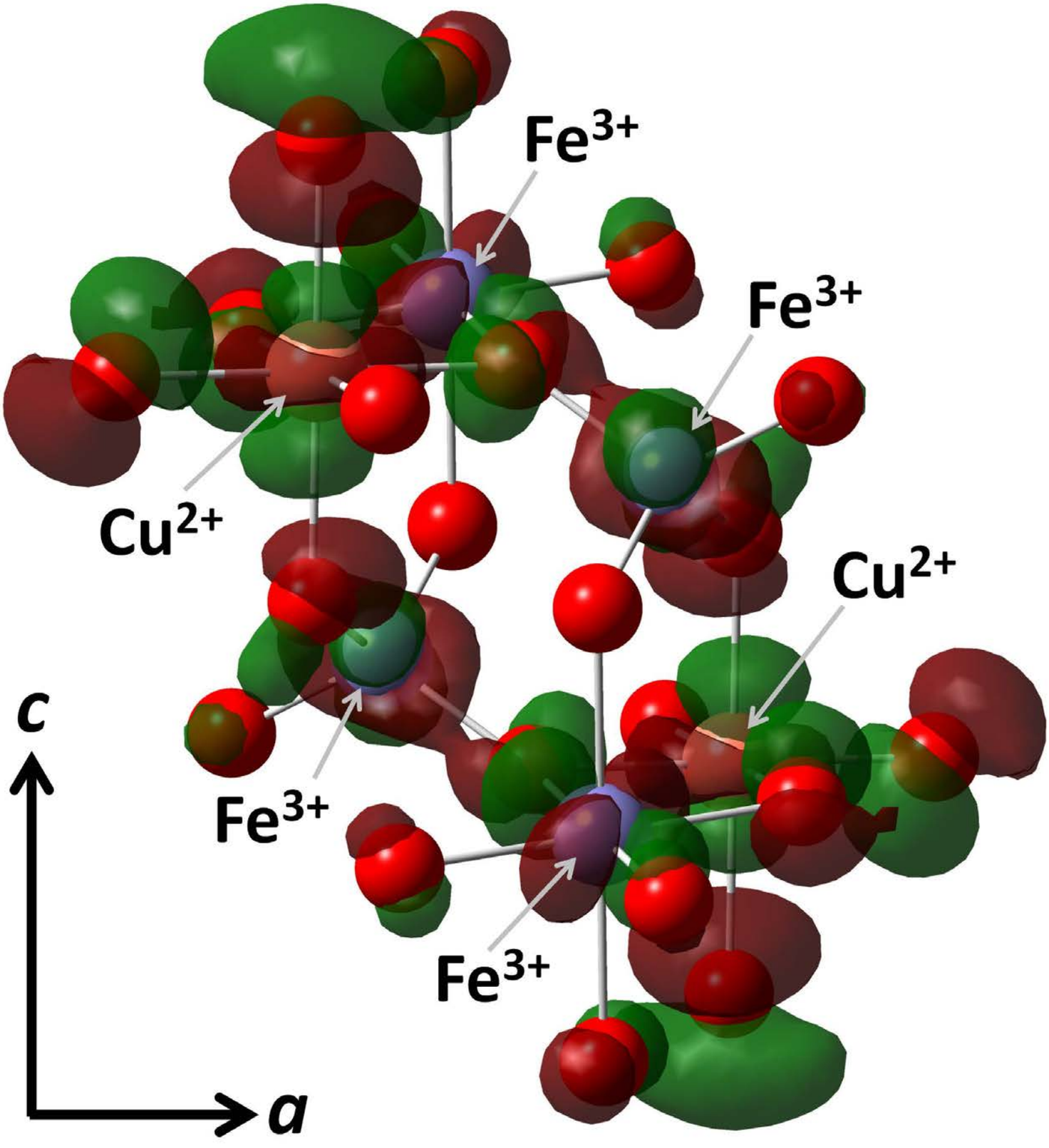

Figure 5. Electronic orbitals in the tetragonally distorted cuprospinel at 4.6 GPa, calculated by *ab initio* method. The red and green colors indicate positive and negative phases in the wave function, respectively. The orbitals are drawn at an isosurface value of 0.02.

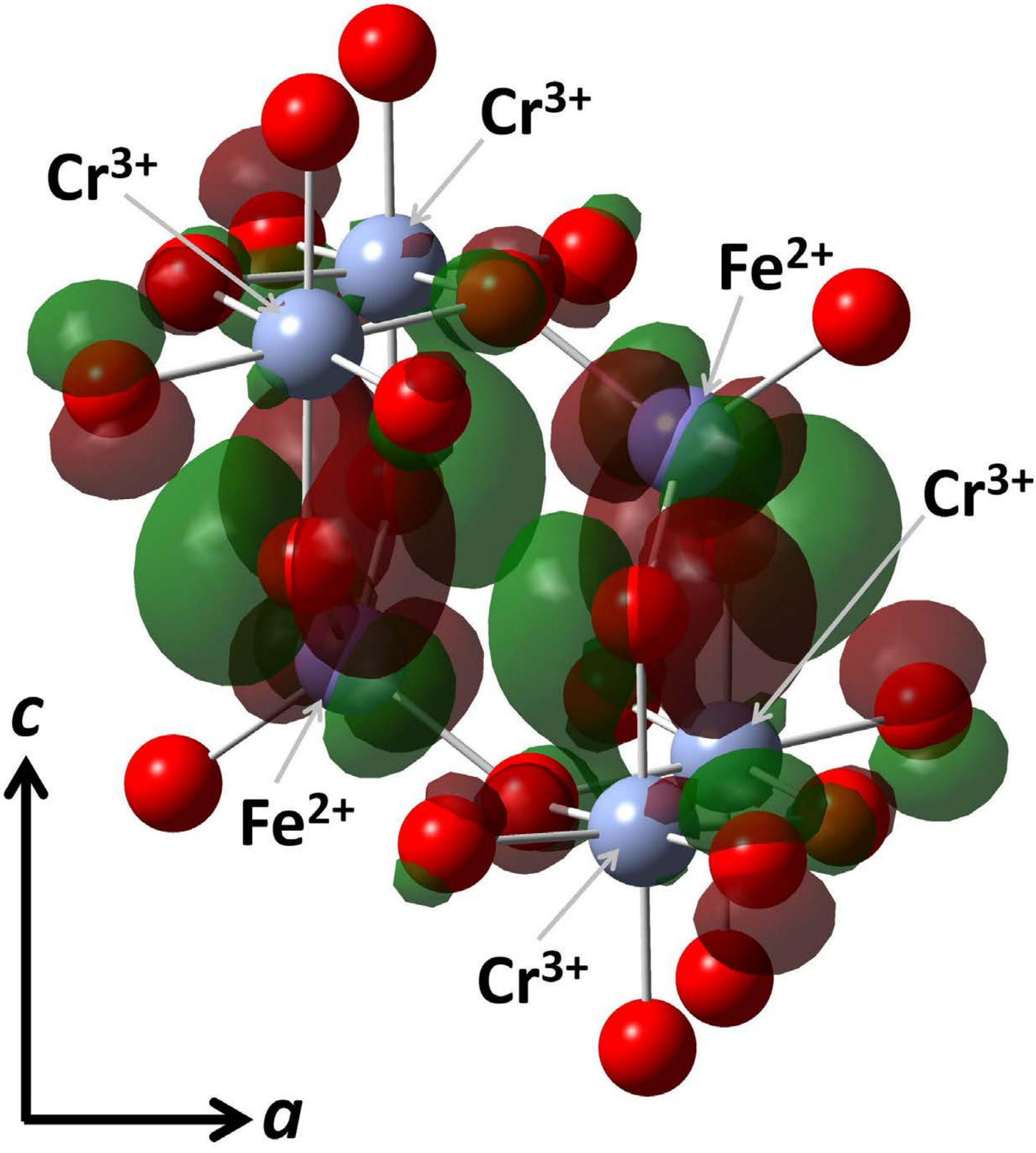

Figure 6. Electronic orbitals in chromite at 13.7 GPa, calculated by *ab initio* method.

This is a preprint, the final version is subject to change, of the American Mineralogist (MSA)
Cite as Authors (Year) Title. American Mineralogist, in press.
(DOI will not work until issue is live.) DOI: http://dx.doi.org/10.2138/am-2015-5224

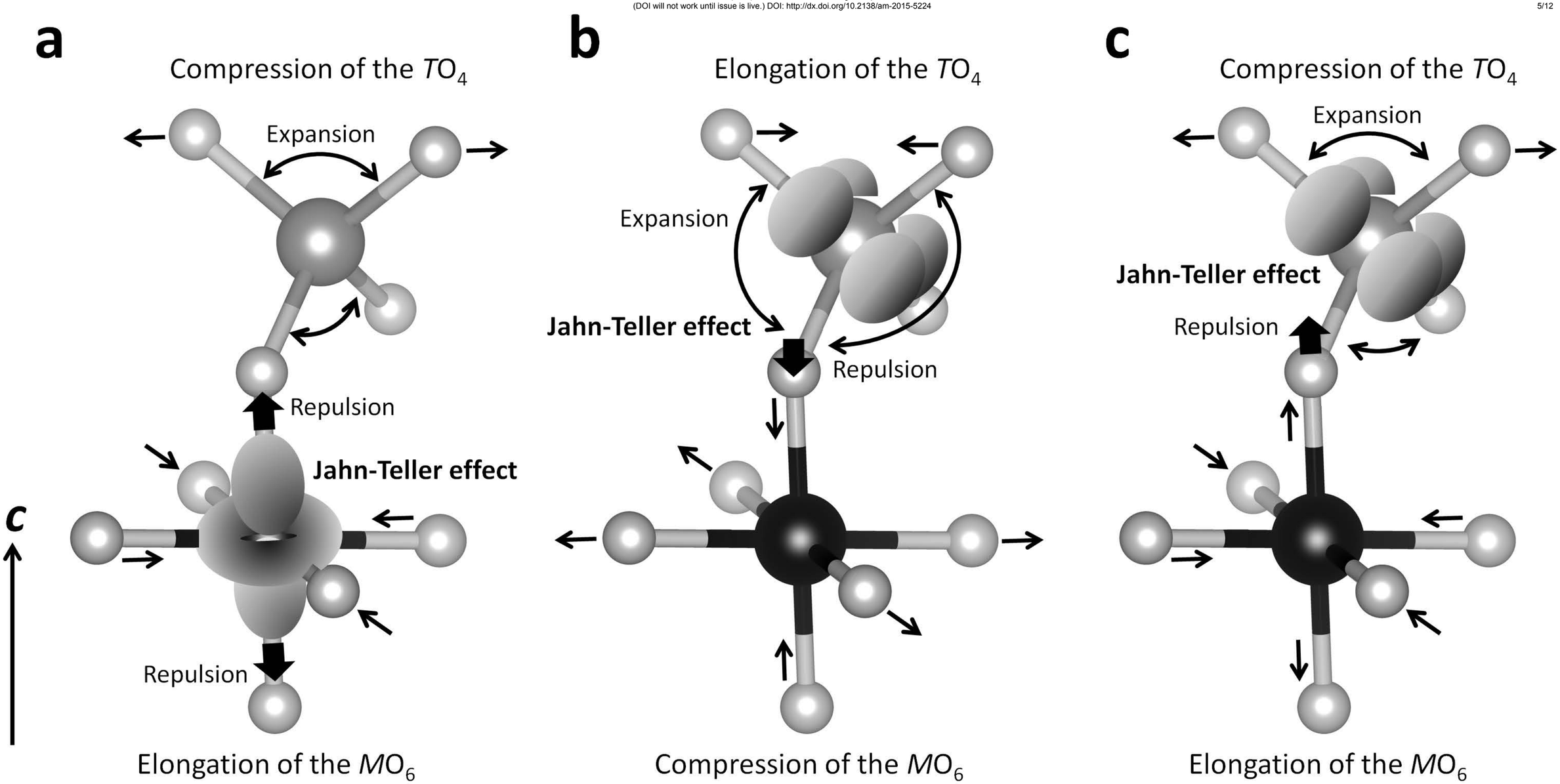

Figure 7 Tetragonally distorted spinel induced by electrostatic repulsion between oxygen ions and the 3*d* orbitals of a Jahn-Teller active cation. Structural deformations caused by (a) elongation of the MO_6 along the *c*-axis in cuprospinel, (b) elongation of the TO_4 along the *c*-axis in chromite and ulvöspinel at high pressure, and (c) compression of the TO_4 along the *c*-axis in chromite at low temperature.

Table 1. Minerals in spinel oxide group (*Fd*-3*m*) with Jahn-Teller active cations under ambient conditions

Mineral name	Furmula	*a* lattice parameter	Octahedral (*M*) site		Tetrahedral (*T*) site		Reference
			cation (apfu)	JT active cation	cation (apfu)	JT active cation	
Hercynite	$FeAl_2O_4$	8.14578(3) Å	$Al_{1.87}Fe^{2+}_{0.13}$	Fe^{2+}	$Fe^{2+}_{0.87}Al_{0.13}$	Fe^{2+}	Harrison et al. (1998)
Magnetite	Fe_3O_4	8.3967(3) Å	$Fe^{2+}_{1.00}Fe^{3+}_{1.00}$	Fe^{2+}	$Fe^{3+}_{1.00}$	-	Bosi et al. (2009)
Cuprospinel	$CuFe_2O_4$	8.389(2) Å	$Fe^{3+}_{1.22}Cu_{0.78}$	Cu^{2+}	$Fe^{3+}_{0.78}Cu_{0.22}$	Cu^{2+}	Lakhani et al. (2011)
Ulvöspinel	Fe_2TiO_4	8.5469(3) Å	$Fe^{2+}_{1.00}Ti_{1.00}$	Fe^{2+}	$Fe^{2+}_{1.00}$	Fe^{2+}	Yamanaka et al. (2009)
Chromite	$FeCr_2O_4$	8.3832(5) Å	$Cr_{2.00}$	-	$Fe^{2+}_{1.00}$	Fe^{2+}	Kyono et al. (2012)
Coulsonite	FeV_2O_4	8.4392(1) Å	$V^{3+}_{2.00}$	V^{3+}	$Fe^{2+}_{1.00}$	Fe^{2+}	Nii et al. (2012)
Vuorelainenite	MnV_2O_4	8.5325(2) Å	$V^{3+}_{2.00}$	V^{3+}	$Mn_{1.00}$	-	Nii et al. (2012)
Magnesiocoulsonit	MgV_2O_4	8.4170(7) Å	$V^{3+}_{1.36}V^{4+}_{0.32}Mg_{0.32}$	V^{3+}, V^{4+}	$Mg_{1.00}$	-	Uchida et al. (2007)

Table 2 Unit cell parameters and volumes for cuprospinel at different pressures

Pressure (GPa)	Crystal system	a (Å)	pseudo-cubic a' (Å)†	c (Å)	c/a'	V (Å^3)	pseudo-cubic V (Å^3)†
0.01	cubic	8.391(3)				590.8(6)	
1.8	cubic	8.364(3)				585.1(6)	
2.7	cubic	8.351(4)				582.3(8)	
3.8	cubic	8.337(4)				579.5(8)	
4.6	tetragonal	5.882(1)	8.318(1)	8.337(1)	1.002	288.5(1)	576.9(2)
5.9	tetragonal	5.867(1)	8.297(2)	8.353(3)	1.007	287.5(2)	575.0(4)

† The a' unit cell parameter and unit cell volume in tetragonal lattice are multiplied by $\sqrt{2}$ and 2, respectively.

Table 3 Structural refinement parameters and crystal structure data for cuprospinel

Pressure (GPa)		0.01	1.8	2.7	4.6
Crystal system		cubic	cubic	cubic	tetragonal
Space group		*Fd-3m*	*Fd-3m*	*Fd-3m*	$I4_1/amd$
Unit cell parameters	a (Å)	8.391(3)	8.364(3)	8.351(4)	5.882(1)
	c (Å)				8.337(1)
No. of collected reflections		100	99	108	109
No. of unique reflections with $F_o > 4\sigma(F_o)$		25	24	26	38
$R1$ (%)		1.60	1.59	2.00	3.32
$wR2$ (%)		2.34	3.65	3.57	7.03
GooF		1.154	1.313	1.200	1.232
T (x, y, z)			(1/8, 1/8, 1/8)		(0, 3/4, 1/8)
Site occupancy fuctor			Fe 0.90(1), Cu 0.10(1)		
M (x, y, z)			(1/2, 1/2, 1/2)		(0, 0, 1/2)
Site occupancy fuctor			Fe 0.75(1), Cu 0.25(1)		
O x		0.2567(2)	0.2562(1)	0.2560(3)	0.0
O y		0.2567(2)	0.2562(1)	0.2560(3)	0.485(1)
O z		0.2567(2)	0.2562(1)	0.2560(3)	0.252(1)
$U_{iso}(T)$ (Å^2)		0.0051(5)	0.0046(8)	0.0031(6)	0.004(1)
$U_{iso}(M)$ (Å^2)		0.0030(4)	0.0036(8)	0.0019(7)	0.006(1)
U_{iso}(O) (Å^2)		0.013(1)	0.015(2)	0.007(1)	0.036(3)
T-O ×4 (Å)		1.915(2)	1.900(1)	1.895(5)	1.886(1)
O-T-O (i) (°)		109.47	109.47	109.47	111.7(7)
O-T-O (ii) (°)		109.47	109.47	109.47	108.4(3)
TO_4 volume (Å^3)		3.60	3.52	3.49	3.44
σ^2_{tet}*		0.00	0.00	0.00	2.91
M-O ×2 (Å)	parallel to c-axis	2.043(2)	2.041(1)	2.039(3)	2.070(9)
M-O ×4 (Å)	parallel to ab-plane	2.043(2)	2.041(1)	2.039(3)	2.017(4)

O-*M*-O × 2 (°)	93.21(8)	92.94(4)	92.8(1)	93.6(3)
O-*M*-O × 4 (°)	93.21(8)	92.94(4)	92.8(1)	92.3(1)
MO_6 volume (Å^3)	11.32	11.29	11.26	11.19
λ_{oct}*	1.000	1.000	1.000	1.001
σ^2_{oct}*	11.24	9.44	8.80	8.52

* Quadratic elongation parameter, λ, and bond angle variance parameter, σ^2, defined by Robinson et al. (1971).

Table 4. Lattice parameters, selected bond distances and angles in cuprospinel, chromite, and ulvöspinel measured at ambient, high pressure and low temperature conditions

Mineral (Formula)	Conditions	S.G.	Lattice parameter			Octahedral (*M*) site								Tetrahedral (*T*) s		
							Bond distance				Bond angle				Bond distance	
			a (Å)	*c* (Å)	*c*/*a*[a] (Elongation[b])	Cations	*M*-O//*c* (Å)	*M*-O//*ab* (Å)	*M*-O ratio (Elongation[b])	λ_{oct}[c]	O-*M*-O//*c* (°)	O-*M*-O//*ab* (°)	σ^2_{oct}[c]	Cations	*T*-O ↔ 4 (Å)	O–*T*–O (i) (°)
Cuprospinel ($CuFe_2O_4$)	Ambient	*Fd*-3*m*	8.391(3)	8.391(3)	1.000	Fe^{3+}	2.043(2)	2.043(2)	1.000	1.000	93.21(8)	93.21(8)	11.24		1.915(2)	109.47
	4.6 GPa	$I4_1/amd$	5.882(1)	8.337(1)	1.002	Cu^{2+}	2.070(9)	2.017(1)	1.026	1.001	92.3(1)	93.6(3)	8.52	Fe^{3+} Cu^{2+}	1.886(1)	111.7(7)
	293 K[d]	$I4_1/amd$	5.81227(4)	8.7115(1)	1.060	Fe^{2+}	2.180(13)	1.990(13)	1.095	1.002	91.8(1)	93.8(1)	7.61		1.892(13)	110(1)
Chromite ($FeCr_2O_4$)	Ambient[e]	*Fd*-3*m*	8.3832(5)	8.3832(5)	1.000		1.997(3)	1.997(3)	1.000	1.000	96.1(2)	96.1(2)	41.13		1.996(6)	109.47
	13.7 GPa[e]	$I4_1/amd$	5.8114(7)	8.1570(51)	0.992	Cr^{3+}	1.904(49)	1.992(21)	0.956	1.001	96(2)	94(1)	33.39	Fe^{2+}	1.934(37)	106.5(19)
	90 K[f]	$I4_1/amd$	5.93(2)	8.26(3)	0.985		1.994(7)	1.989(5)	1.003	1.000	95.6(1)	96.6(1)	35.47		1.982(5)	111.8(1)
Ulvöspinel (Fe_2TiO_4)	Ambient[g]	*Fd*-3*m*	8.5297(3)	8.5297(3)	1.000		2.0421(9)	2.0421(9)	1.000	1.000	95.4(3)	95.4(3)	31.81		2.0107(9)	109.47
	11.4 GPa[g]	$I4_1/amd$	5.930(1)	8.284(1)	0.988	Fe^{2+} Ti^{4+}	1.995(2)	2.025(7)	0.985	1.000	95.1(5)	94.4(5)	25.96	Fe^{2+}	1.961(9)	108.3(6)
	103 K[g]	$I4_1/amd$	6.006(4)	8.525(3)	1.004		2.044(2)	2.041(2)	1.001	1.000	94.9(1)	95.0(1)	27.27		1.995(2)	109.1(1)

[a] The *a* lattice parameter of body centered tetragonal lattice is multiplied by $\sqrt{2}$.

[b] As the ratio is larger than 1.000, the geometry of unit cell lattice, the octahedral coordination, and the tetrahedral coordination is elongated along the *c*-axis.

[c] Quadratic elongation parameter, λ, and bond angle variance parameter, σ^2, defined by Robinson et al. (1971).

[d] Balagurov et al. (2013)

[e] Kyono et al. (2012)

[f] Tsuda et al. (2010)

[g] Yamanaka et al. (2009)

ite	
Bond angle	
109.47/O-*T*-O (i) (Elongation[b])	σ^2_{tet} [c]
1.000	0.00
0.980	2.91
0.995	0.01
1.000	0.00
1.028	5.40
0.979	3.46
1.000	0.00
1.011	0.22
1.003	0.06